Title

Electrolytic synthesis of aqueous aluminum nanoclusters and in situ characterization by femtosecond Raman spectroscopy and computations.

Journal

Proceedings of the National Academy of Sciences of USA, 110(46)

Authors

Wang, Wei
Liu, Weimin
Chang, I-Ya
et al.

Publication Date

2013-11-12

DOI

10.1073/pnas.1315396110

Peer reviewed

Electrolytic synthesis of aqueous aluminum nanoclusters and in situ characterization by femtosecond Raman spectroscopy and computations

Wei Wang[a,1], Weimin Liu[a,1], I-Ya Chang[a,1], Lindsay A. Wills[a], Lev N. Zakharov[a], Shannon W. Boettcher[b], Paul Ha-Yeon Cheong[a,2], Chong Fang[a,2], and Douglas A. Keszler[a,2]

[a]Department of Chemistry, Oregon State University, Corvallis, OR 97331-4003; and [b]Department of Chemistry, University of Oregon, Eugene, OR 97403-1253

Edited by Harry B. Gray, California Institute of Technology, Pasadena, CA, and approved October 8, 2013 (received for review August 13, 2013)

The selective synthesis and in situ characterization of aqueous Al-containing clusters is a long-standing challenge. We report a newly developed integrated platform that combines (*i*) a selective, atom-economical, step-economical, scalable synthesis of Al-containing nanoclusters in water via precision electrolysis with strict pH control and (*ii*) an improved femtosecond stimulated Raman spectroscopic method covering a broad spectral range of *ca.* 350–1,400 cm^{-1} with high sensitivity, aided by ab initio computations, to elucidate Al aqueous cluster structures and formation mechanisms in real time. Using this platform, a unique view of *flat* $[Al_{13}(\mu_3\text{-}OH)_6(\mu_2\text{-}OH)_{18}(H_2O)_{24}](NO_3)_{15}$ nanocluster formation is observed in water, in which three distinct reaction stages are identified. The initial stage involves the formation of an $[Al_7(\mu_3\text{-}OH)_6(\mu_2\text{-}OH)_6(H_2O)_{12}]^{9+}$ cluster core as an important intermediate toward the *flat* Al_{13} aqueous cluster.

Al aqueous speciation | ultrafast Raman | computational chemistry | electrochemistry | reaction pathway

The importance of Al (aluminum) in the biosphere and to human civilization is enormous. The scale of mining and production of Al compounds is second only to that of Fe (iron). Our lives are influenced by its use in electronics (1, 2), cooking and eating utensils, and food packaging, and as structural materials in the construction, automotive, and aircraft industries. Its deposition and migration as a mineral ore are controlled by its aqueous chemistry and speciation. Millions of tons of Al compounds are used worldwide each year for water treatment, and it is found in all drinking water (3). The behavior of Al in water plays significant roles in soil chemistry and plant growth (4, 5), for example, governing Al bioavailability, toxicity, and its overall impact in aquatic ecosystems (6). Meanwhile, aqueous Al clusters are gaining importance as solution precursors for the large-area deposition of Al_2O_3 coatings with broad technological applications (7, 8).

Despite more than a century of study (9, 10), the complete portrait of aqueous Al chemistry remains unclear. Studies of aqueous Al chemistry are notoriously difficult because of the variety and complexity of the species that can be formed, encompassing monomeric, oligomeric, and polymeric hydroxides (11–17); colloidal solutions and gels; and precipitates. Synthesis is complicated by the fact that the counter-ions and the method and rate of pH change all have dramatic effects on product formation (18, 19). Few methods exist for the in situ determination and assignment of molecular-level structures. For instance, ^{27}Al NMR can only identify certain Al aqueous species (15). Furthermore, unlike organic compounds, systematic spectroscopic signatures of metal hydroxide clusters are less accessible, making interpretation of experimental spectra challenging. We hereby report a combined synthesis, experiment, and theory platform for the study of aqueous metal clusters. Electrolysis is exploited to control the solution pH and counter-ion content precisely during cluster synthesis without using chemical reagents. The evolution of solution species is followed in situ by an improved femtosecond stimulated Raman (FSR) technique (20–22) that can detect weak signals associated with structure-defining vibrational modes. The resulting pH-dependent Raman spectra are interpreted by juxtaposition to quantum mechanically computed vibrational modes to assign specific molecular structures. Through this integrated approach, we have discovered a speciation behavior for Al in water that has not previously been observed. We focus here on the synthesis and formation pathway of the *flat* $[Al_{13}(\mu_3\text{-}OH)_6(\mu_2\text{-}OH)_{18}(H_2O)_{24}]^{15+}$ cluster (Al_{13}) that is practically important for its use as a "green" solution precursor for the large-scale/large-area preparation of Al_2O_3 thin films and nanoparticles that have broad utility in electronics, catalysis, and corrosion prevention (7, 8, 23–27).

Results and Discussion

Although the *flat* cluster $[Al_{13}(\mu_3\text{-}OH)_6(\mu_2\text{-}OH)_{18}(H_2O)_{24}]^{15+}$ is commonly considered a minor component in Al speciation that does not appear in published predominance (i.e., Pourbaix) diagrams (28, 29), it can now be synthesized in large quantities (30–32). Here, we demonstrate complete atom economy and step economy in the selective synthesis of the Al_{13} cluster using

Significance

The aqueous chemistry of Al has a large impact across the biosphere, hydrosphere, geosphere, and anthrosphere. Despite a century of study, aqueous Al chemistry and speciation are still not well understood because of the challenges of selectively isolating and synthesizing specific Al-containing aqueous clusters and of precisely characterizing those clusters. We report the atom- and step-economical electrolytic synthesis of aqueous Al clusters combined with improved femtosecond Raman spectroscopy and computations to elucidate the structures and formation pathways of aqueous clusters in situ. We demonstrate the unique power of this integrated platform by synthesizing and characterizing *flat* $[Al_{13}(\mu_3\text{-}OH)_6(\mu_2\text{-}OH)_{18}(H_2O)_{24}]^{15+}$ clusters in water, which are versatile precursors for large-scale preparation of Al_2O_3 thin films and nanoparticles for electronics, catalysis, and corrosion prevention.

Author contributions: S.W.B., P.H.-Y.C., C.F., and D.A.K. designed research; W.W. and S.W.B. developed the electrochemical methods; W.L. and C.F. developed the new femtosecond stimulated Raman capabilities; W.W., W.L., I.-Y.C., L.A.W., L.N.Z., and C.F. performed research; I.-Y.C., L.A.W., and P.H.-Y.C. performed the computations; W.W., W.L., S.W.B., C.F., and D.A.K. contributed new reagents/analytic tools; L.N.Z. contributed to the single crystal X-ray diffraction; W.W., I.-Y.C., L.A.W., and C.F. analyzed data; and W.W., W.L., I.-Y.C., S.W.B., P.H.-Y.C., C.F., and D.A.K. wrote the paper.

The authors declare no conflict of interest.

This article is a PNAS Direct Submission.

Freely available online through the PNAS open access option.

[1]W.W., W.L., and I.-Y.C. contributed equally to this work.

[2]To whom correspondence may be addressed. E-mail: paulc@science.oregonstate.edu, chong.fang@oregonstate.edu, or douglas.keszler@oregonstate.edu.

This article contains supporting information online at www.pnas.org/lookup/suppl/doi:10.1073/pnas.1315396110/-/DCSupplemental.

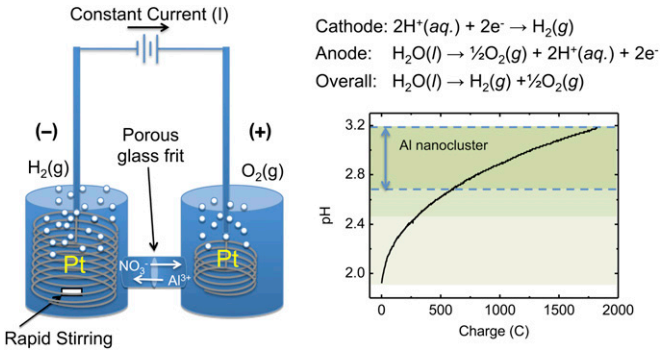

Fig. 1. (*Left*) Cell for $Al(NO_3)_3$ (*aq*) electrolysis. (*Right*) Balanced reactions under acidic conditions are shown in the upper part of the graph. Cathode solution pH vs. total charge passed through the system is shown in the lower part of the graph; the region of Al nanocluster formation is highlighted.

an electrochemical method to increase the pH of a 1.0-M $Al(NO_3)_3$ (*aq*) solution smoothly.

The predominant Al species in a 1.0-M $Al(NO_3)_3$ (*aq*) solution is the monomeric hexa-aqua ion $Al(H_2O)_6^{3+}$ (*aq*) (33). As the pH of the solution increases, condensation of the monomeric ion occurs, leading to the formation of polynuclear Al hydroxide clusters. To prevent the steep pH gradients commonly associated with base titrations, the pH change is achieved by proton reduction in a two-compartment electrochemical cell (Fig. 1). In the cathode compartment, protons are reduced to hydrogen gas, increasing the pH. In the anode compartment, water oxidation results in a decrease in pH. The reaction rate is controlled by adjusting the electrical current through the cell. A porous glass frit eliminates convective mixing between the two compartments. Because the NO_3^- and $Al(H_2O)_6^{3+}$ are present in large concentrations (i.e., ~3.0 and 1.0 M, respectively) relative to H^+ in the pH range explored, the bulk of the charge-balancing ionic current across the frit is carried by NO_3^- migration into the anode compartment and $Al(H_2O)_6^{3+}$ migration into the cathode compartment. The pH of the cathode compartment is plotted against total charge passed in Fig. 1. In this study, we primarily focus on the highlighted range of pH = 2.70–3.18, because it covers the crucial steps for initial formation of Al hydroxide nanoclusters.

The Keggin Al_{13} hydroxide cluster is the most commonly observed polynuclear species in pH-based speciation studies (18, 19). The Keggin structure is characterized by a core, tetrahedral AlO_4 unit surrounded by 12 AlO_6 octahedra. A solution ^{27}Al NMR spectrum (*SI Appendix*, Fig. S1) of the final cathode solution (pH = 3.18) indicates only a minor presence of Al atoms in a tetrahedral site associated with the Keggin Al_{13} structure. Consistent with this observation, we find that all crystals obtained from cathode solutions in the pH range of 2.60–3.10 exhibit unit-cell parameters (*SI Appendix*, Table S1) equivalent to that of the *flat* Al_{13} cluster $[Al_{13}(\mu_3\text{-}OH)_6(\mu_2\text{-}OH)_{18}(H_2O)_{24}]^{15+}$. This cluster contains only distorted octahedral AlO_6 groups, lacking the tetrahedral AlO_4 core of the Keggin cluster. The ease of isolating the *flat* cluster points to the efficacy of the electrolysis method for selective synthesis through precision pH control (32). The electrolysis method is also especially well suited for in situ analysis because of the lack of any additional reagents.

To monitor the formation of the *flat* Al_{13} cluster as a function of pH, the cathode solution is studied in situ by nonresonant (800 nm) FSR spectroscopy (21) with a newly developed Raman probe pulse. The probe pulse is selected from one of the cascaded four-wave mixing (CFWM) signals generated by crossing two femtosecond near-IR laser pulses in one thin transparent medium, providing good spatial separation between self-compressed multicolor sideband lasers (34) and the fundamental beams for ultrabroad spectral coverage (22) (*SI Appendix*, Fig. S2). This unique approach enables the measurement of stimulated Raman signals to frequencies as low as 350 cm^{-1}, significantly extending established low-frequency detection limits, *ca.* 600–800 cm^{-1}, of conventional probe-light generation in FSR spectroscopy. To capture subtle spectral changes and correct for the effects of laser fluctuations, the spectrum of a control 1.0-M $Al(NO_3)_3$ (*aq*) solution was acquired before measuring each pH-specific sample.

The resulting differential FSR spectra (i.e., the differences between sample and control measurements) across the pH range of 1.9–3.18 are shown in Fig. 2. In these spectra, negative peaks represent species being consumed, whereas positive peaks represent new species emerging at the cathode. Three pronounced negative peaks appear at 525 (Al-O stretching of $[Al(H_2O)_6]^{3+}$), 718, and 1,048 cm^{-1} (NO_3^- vibrations) (33). Positive peaks, associated with polynuclear Al clusters, are centered at 386, 585, 675, 777, 937, 1,151, and 1,275 cm^{-1}. Although these Raman peaks are weak, mainly due to high symmetry and small polarizabilities of the Al nanoclusters, their signal-to-noise ratios are statistically significant (*SI Appendix*). The peak located near 1,006 cm^{-1} can be resolved by least-squares peak fitting with multiple Gaussians. Because it partially overlaps with the intense negative peak at 1,048 cm^{-1}, there is considerable uncertainty in assigning a precise position in the differential spectrum; hence, it has not been used in the ensuing analyses.

To identify the individual Raman vibrational modes that constitute each of the peaks in the differential FSR spectrum in

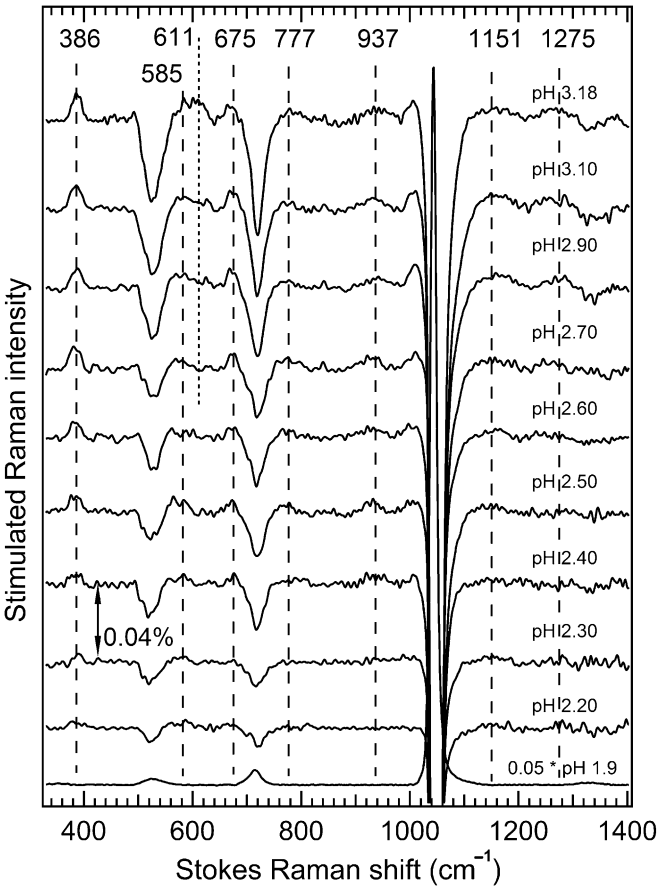

Fig. 2. Differential FSR spectra of the cathode solution as pH increases from 1.90 to 3.18. The vertical double-headed arrow indicates a stimulated Raman gain of 0.04%. The FSR spectrum of the precursor solution (pH = 1.9) is scaled by a factor of 0.05 and plotted at the bottom for comparison. The nascent Raman peaks during reaction are marked by dashed lines.

Fig. 2, least-squares fitted computed (LSFC) Raman spectra were created from the Raman frequencies and intensities of model nanocluster species (35) computed by the Hartree-Fock (HF) method with 6-31G(d,p) basis set (36, 37). All the computations were undertaken with the integral-equation formalism polarizable continuum model (IEFPCM) for aqueous solution and universal force field (UFF) van der Waals radii (38, 39). Results for pH = 3.18 are summarized in Fig. 3. The region from 900–1,300 cm^{-1} exhibits resolved hydroxo group vibrations that collectively define fingerprints for the clusters. We classify these vibrations into three types: μ_3-OH, μ_2-OH_{core}, and μ_2-OH_{shell}, where the subscripts of μ denote the number of Al atoms bound to each hydroxo group. $[Al_7(\mu_3\text{-}OH)_6(\mu_2\text{-}OH)_6(H_2O)_{12}]^{9+}$ (Al_7) represents the planar core of the *flat* Al_{13}: It contains a central Al atom that is bridged to six next nearest-neighbor Al atoms by μ_3-OH groups (red circle in Fig. 3*E*). These groups give rise to signals near 937 and 1,006 cm^{-1}. The outer six Al atoms are also connected to each other by μ_2-OH_{core} bridges (yellow circle in Fig. 3*E*), producing bands near 1,075 and 1,151 cm^{-1}. The *flat* Al_{13} exhibits the Al_7 core with six additional Al atoms appended via μ_2-OH_{shell} linkages. These groups (blue circle in Fig. 3*C*), produce signals near 1,190 and 1,275 cm^{-1}. Mixed bands, comprising both μ_3-OH and μ_2-OH vibrations, are also observed for the Al_{13} cluster near 1,075 and 1,270 cm^{-1}. The structural form of these hydroxo groups is replicated in Al_{7+1} (Fig. 3*D*), where one additional Al atom is appended to the Al_7 core.

Deconvolution of the total LSFC spectrum (Fig. 3*A*) reveals that the solution contains the *flat* Al_{13} cluster as well as the Al_7 species (see Fig. 3 *A*, *C*, and *E*). The peaks near 1,000 and 1,151 cm^{-1} provide strong evidence for the existence of Al_7; the peak at

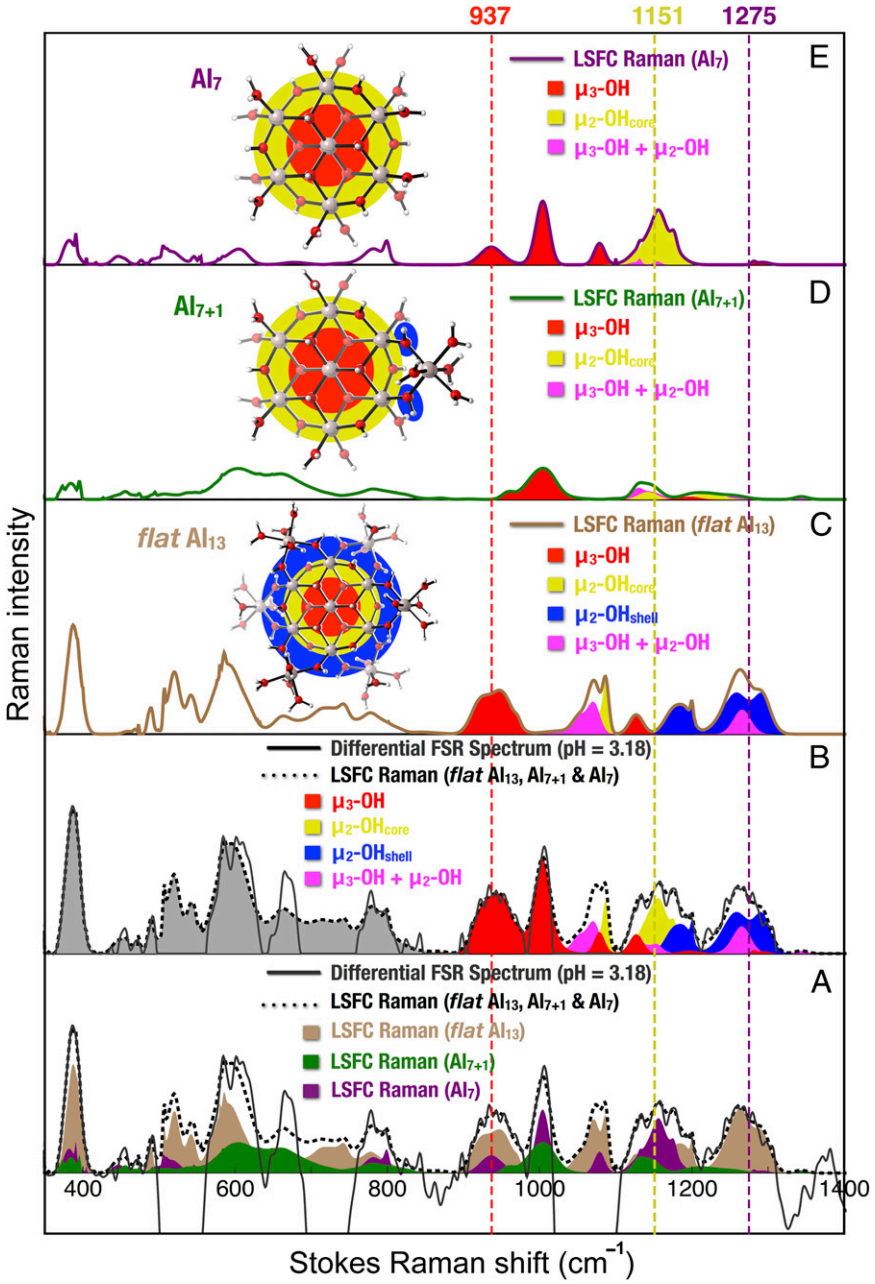

Fig. 3. Differential FSR spectra (pH = 3.18) from each cluster (*A*) and each hydroxyl ligand (*B*) and LSFC spectra of *flat* Al_{13} (*C*, orange), Al_{7+1} (*D*, green), and Al_7 (*E*, violet).

1,151 cm^{-1} is uniquely associated with the μ_2-OH_{core} in Al_7 (Fig. 3*E*). In addition, the Al_{7+1} species $[Al_8(\mu_3\text{-}OH)_6(\mu_2\text{-}OH)_8(H_2O)_{14}]^{10+}$ can be added to the spectrum without negatively affecting the fit, suggesting it likely exists in the solution. The total computed spectrum, incorporating the aforementioned three clusters, correlates well to the differential FSR spectrum over the entire frequency range of *ca.* 350–1,400 cm^{-1} (Fig. 3 *A* and *B*). Computations also reveal that Al-O vibrations dominate in the region from 350–900 cm^{-1}. The rise in the positive signal at ∼386 cm^{-1} is thus a strong and unique indication of Al cluster formation with increasing pH.

To follow the assembly pathway of the Al aqueous clusters, the integrated areas of the 525, 718, and 1,048-cm^{-1} negative peaks and of the 937, 1,151, and 1,275-cm^{-1} positive peaks in Fig. 2 have been normalized and plotted against solution pH in Fig. 4. Three reaction stages are revealed. In stage I (pH = 2.20–2.45), both the NO_3^- and $[Al(H_2O)_6]^{3+}$ concentrations decrease in the cathode solution. The decreasing $[Al(H_2O)_6]^{3+}$ concentration is directly correlated to the formation of Al clusters (increasing 937 and 1,151 cm^{-1} signals) and the concomitant decrease of the NO_3^- concentration (718 and 1,048 cm^{-1}); NO_3^- migrates from the cathode to the anode compartment to maintain the charge balance. As noted above, the 1,151-cm^{-1} peak is uniquely associated with the μ_2-OH_{core} in Al_7 (Fig. 3). Because no significant intensity is detected in the spectral region around 1,275 cm^{-1} corresponding to the μ_2-OH_{shell} of *flat* Al_{13}, we associate this initial reaction stage with the formation of the Al_7 core structure.

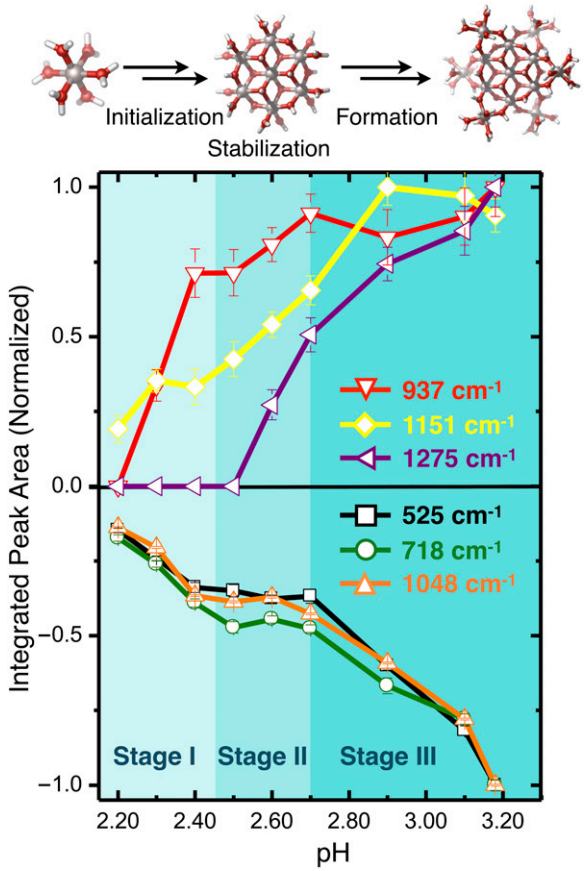

Fig. 4. Differential FSR signal intensity vs. pH for 1.0-M $Al(NO_3)_3$ (*aq*) solution in reaction. Peak assignments for the Al clusters are 937 cm^{-1} (μ_3-OH), 1,151 cm^{-1} (μ_2-OH_{core}), and 1,275 cm^{-1} (μ_2-OH_{shell} and μ_3-OH + μ_2-OH). The signal at 525 cm^{-1} corresponds to Al-O vibrations in $Al(H_2O)_6^{3+}$, and the signals at 718 cm^{-1} and 1,048 cm^{-1} are associated with NO_3^-. The error bar represents 1 SD from the individual mode intensity average of multiple independent measurements on the Al speciation in water (*SI Appendix*, Fig. S3). (*Upper*) Proposed three-stage reaction pathways to form the *flat* Al_{13} via an Al_7 intermediate are delineated.

In stage II (pH = 2.45–2.70), the Al_7 cluster continues to dominate, but the appearance and growth of the 1,275-cm^{-1} signal uniquely indicate the formation of the Al_{13} cluster. There is little change in the NO_3^- and $[Al(H_2O)_6]^{3+}$ concentrations across this region, suggesting a predominance of hydrolysis, stabilization, and condensation of Al species in response to the pH change. The continuously rising 1,151-cm^{-1} signal in concert with the 1,275-cm^{-1} peak is a clear indication that Al_7 and Al_{13} concentrations are increasing. Intermediate species, such as Al_{7+1}, may also be forming, but assignments here are less certain. Moreover, the Al_{7+1} structure is probably only one of a set of sequential species Al_{7+n} (n = 1–5) contributing to initial formation of *flat* Al_{13}.

In stage III (pH = 2.70–3.18), the increasing 1,275-cm^{-1} signal is consistent with a continuing shift of equilibria favoring *flat* Al_{13}. The 937- and 1,151-cm^{-1} signals are associated with both Al_7 and Al_{13}, and no significant changes are expected as the equilibrium shifts; hence, the plateau in these spectral signatures is explained. This stage also covers the pH range where crystals of *flat* Al_{13} nitrate can most readily be harvested from the cathode solution. Both the NO_3^- and $[Al(H_2O)_6]^{3+}$ signals decrease to a larger extent than that in stage I, representing further nitrate migration from the cathode as the reaction progresses toward building larger Al nanoclusters.

Conclusion

The combined techniques described herein are a powerful toolset for the synthesis and analysis of aqueous metal clusters. The single-reagent electrolytic synthesis provides precise control of product selectivity and scalability. The smoothly varying pH eliminates the sharp gradients that may lead to nucleation of the tetrahedral AlO_4 species at low apparent pH values, while also enabling the in situ study, isolation, and crystallization of *flat* Al_{13} in a clean and efficient way. The femtosecond spectroscopic approach provides an effective means to establish both chemical identity and detailed molecular structure for a metal species in water, corroborated by systematic computations for structural-mode assignment. We have demonstrated the power of this integrated approach by providing a vivid view of aqueous Al chemistry in action, which extends the highly cited Al predominance diagrams by quantifying and elucidating a unique three-stage formation pathway for the important *flat* Al_{13} cluster via an Al_7 intermediate. The proposed condensation pathway, involving only octahedrally coordinated Al, is also consistent with the existence and structures of the common minerals gibbsite and boehmite, which contain Al only in distorted octahedral coordination environments.

Taken together, this report provides unique insights and tools concerning the nature of the equilibria and intermediates contributing to the complex condensation and speciation chemistries of Al, while raising questions about behavior outside the pH range studied here. The methods open a new chapter in the study of Al, a biologically and technologically important element, and also provide a general approach for establishing the molecular structures of species in other aqueous metal systems.

Materials and Methods

Electrochemical Synthesis. The 1.0-M $Al(NO_3)_3$ (*aq*) starting solution was made with $Al(NO_3)_3{\cdot}9H_2O$ (American Chemical Society grade; Baker Analyzed Reagent) and ultrapure water (ρ = 18.2 MΩ·cm). Constant current bulk electrolysis was carried out using an EG&G 263A potentiostat in two-electrode mode with the reference electrode input lead connected to the counter-electrode. A custom-built, two-compartment cell comprising a 15-mL cathode, a 50-mL anode, and a standard medium porosity glass frit (Chemglass) to separate the two compartments was used. The solution volumes in the cathode and anode were 10 mL and 30 mL, respectively. Pt (platinum) wire coils were used for both electrodes. To minimize local pH gradients in the cathode compartment where the cluster is synthesized, the cathode solution was stirred rapidly during electrolysis and a large-surface area (23 cm^2) Pt wire coil was used as the working electrode. The current was set to 75 mA during the experiment, which required *ca.* 4 V across the working and counterelectrodes due to the kinetic overpotentials associated with the

hydrogen and oxygen evolution reactions, as well as the series resistance of the two-compartment cell. The charge Q was determined by $Q = I{\cdot}t$. No significant temperature changes were observed during the prolonged electrolysis reaction, consistent with the low-power dissipation (75 mA × ~4 V = 0.3 W). The pH of the cathode compartment solution was monitored in real time using an ion-sensitive field-effect transistor pH probe. Upon reaching the desired pH, the cathode solution was directed into a flow cell for the in situ FSR spectroscopic measurements.

Improved FSR Spectroscopy. The FSR spectroscopic setup consists of a mode-locked Ti:sapphire oscillator (Mantis-5) and regenerative amplifier (Legend Elite-USP-1K-HE; Coherent), which provides 35-fs, 800-nm pulses with ~4.1 mJ per pulse energy at a repetition rate of 1 kHz. The fundamental beam of ~1.6 mJ per pulse energy is dispersed by a reflective grating (1,200 grooves per millimeter, 750-nm blaze) and passed through a 90-μm wide slit to generate the Raman pump of ~10-cm^{-1} bandwidth and ~3.5-ps pulse duration. The Raman probe represents an advancement of conventional methods, which originates from CFWM sideband signals generated by crossing two laser pulses [the 800-nm beam (~35 fs, 3 μJ per pulse) and the IR component of the supercontinuum white light generated in a 2-mm thick sapphire plate followed by prism compression (~45 fs, 100 nJ per pulse)] in a 0.1-mm thick β-barium borate crystal (type I, $\theta = 27.8°$) (22, 34). The incident beam diameters on the crystal are ~0.2 mm, and the crossing angle is ~6°. One of the CFWM signals with an ~900-nm center wavelength is selected as the Raman probe, corresponding to the Stokes frequency range from *ca.* 100–3,000 cm^{-1} and a pulse duration of ~30 fs. The Raman pump and probe beams are then focused onto the 1-mm pathlength sample flow cell by an off-axis parabola (to avoid pulse chirp). Only the transmitted probe beam carrying the stimulated Raman signal enters the spectrograph to be dispersed by a 600-grooves-per-millimeter grating (1,000-nm blaze) and imaged onto a CCD camera (PIXIS 100F; Princeton Instruments), which consists of a 1,340 × 100-pixel array and is synchronized with the laser repetition. Each sample spectrum is averaged from 180,000 Raman spectra within ~6 min, and the 1.0-M $Al(NO_3)_3$ precursor solution spectrum is collected in exactly the same manner right before each pH-specific sample solution measurement as the standard for NO_3^- mode intensity normalization and generation of the differential FSR spectra (Fig. 2). Both the spectral dips and peaks in the differential spectra are multi-Gaussian least-squares fitted across the wide spectral range (21), and the integrated peak areas are plotted vs. pH to capture the real-time evolution of the broad signal intensity during electrolysis.

Computations. The geometries and spectra of the Al clusters of interest (*SI Appendix*, Fig. S4) were computed using HF/6-31G(d,p) with the IEFPCM-UFF continuum solvation model for water at the electronic ground state (36–39).

Least-Squares Fitting Procedure.

i) Each computed Raman vibrational mode was mathematically described with a Gaussian function using the computed Raman vibrational frequency and intensity. A frequency parameter (F) was used to modulate the frequencies of all species, amplitude parameters (A_i) for the amplitude of each species, and width parameters (W_{ij}) for the width of each Gaussian. The sum of all Gaussian curves constitutes the LSFC Raman spectrum.

ii) The parameters (F, A_i, and W_{ij}) were then iterated to minimize the rmsd between the trial LSFC Raman spectrum and the experimental spectrum. The vibrational modes of all eliminated peaks were checked and verified manually for chemical relevance.

iii) The individual Gaussians in the final LSFC Raman spectra can then be identified according to the functional groups and partitioned as shown in Fig. 3.

ACKNOWLEDGMENTS. Financial support was provided by the National Science Foundation (Grant CHE-1102637), by Vicki and Patrick F. Stone (P.H.-Y.C.), by the Oregon State University (OSU) Ingram Fellowship (to L.A.W.), and by the OSU College of Science Venture Development Fund and OSU Faculty Research Startup Fund (to C.F.).

1. Robertson J (2006) High dielectric constant gate oxides for metal oxide Si transistors. *Rep Prog Phys* 69(2):327–396.
2. Schmidt J, et al. (2008) Surface passivation of high-efficiency silicon solar cells by atomic-layer-deposited Al_2O_3. *Prog Photovolt Res Appl* 16(6):461–466.
3. World Health Organization (2011) *Guidelines for Drinking Water Quality* (World Health Organization, Geneva).
4. Delhaize E, Ryan PR (1995) Aluminum toxicity and tolerance in plants. *Plant Physiol* 107(2):315–321.
5. Bohn HL, McNeal B, O'Connor G (2001) *Soil Chemistry* (Wiley, New York).
6. Gensemer RW, Playle RC (1999) The bioavailability and toxicity of aluminum in aquatic environments. *Crit Rev Environ Sci Technol* 29(4):315–450.
7. Meyers ST, et al. (2007) Solution-processed aluminum oxide phosphate thin-film dielectrics. *Chem Mater* 19(16):4023–4029.
8. Keszler DA, Wang W, inventors; State of Oregon, assignee. 2013 April 4. Process to form aqueous precursor and aluminum oxide film. United States patent US 13/703,592.
9. Kablukov I, Sachanov AZ (1910) The hydrolytic and electrolytic dissociation of aluminum bromide. *Z Physik Chem* 69:419–432.
10. Heyrovský J (1920) The electroaffinity of aluminium. Part I. The ionisation and hydrolysis of aluminium chloride. *Journal of the Chemical Society, Transactions* 117:11–26.
11. Johansson G, Lundgren G, Sillén LG, Söderquist R (1960) On the crystal structure of a basic aluminum sulfate and the corresponding selenate. *Acta Chem Scand* 14:769–771.
12. Johansson G (1962) The crystal structures of $[Al_2(OH)_2(H_2O)_8](SO_4)_2{\cdot}2H_2O$ and $[Al_2(OH)_2(H_2O)_8](SeO_4)_2{\cdot}2H_2O$. *Acta Chem Scand* 16:403–420.
13. Allouche L, Gérardin C, Loiseau T, Férey G, Taulelle F (2000) Al_{30}: A giant aluminum polycation. *Angew Chem Int Ed Engl* 39(3):511–514.
14. Rowsell J, Nazar LF (2000) Speciation and thermal transformation in alumina sols: Structures of the polyhydroxyoxoaluminum cluster $[Al_{30}O_8(OH)_{56}(H_2O)_{26}]^{18+}$ and its δ-Keggin moieté. *J Am Chem Soc* 122(15):3777–3778.
15. Casey WH, Phillips BL, Furrer G (2001) Aqueous aluminum polynuclear complexes and nanoclusters: A review. *Reviews in Mineralogy and Geochemistry* 44:167–190.
16. Casey WH, Olmstead MM, Phillips BL (2005) A new aluminum hydroxide octamer, $[Al_8(OH)_{14}(H_2O)_{18}](SO_4)_5{\cdot}16H_2O$. *Inorg Chem* 44(14):4888–4890.
17. Casey WH (2006) Large aqueous aluminum hydroxide molecules. *Chem Rev* 106(1):1–16.
18. Akitt JW, Farthing A (1981) Aluminium-27 nuclear magnetic resonance studies of the hydrolysis of aluminium(III). Part 4. Hydrolysis using sodium carbonate. *J Chem Soc Dalton Trans* 1981:1617–1623.
19. Hu C, Liu H, Qu J (2005) Preparation and characterization of polyaluminum chloride containing high content of Al_{13} and active chlorine. *Colloids Surf A Physicochem Eng Asp* 260:109–117.
20. Frontiera RR, Fang C, Dasgupta J, Mathies RA (2012) Probing structural evolution along multidimensional reaction coordinates with femtosecond stimulated Raman spectroscopy. *Phys Chem Chem Phys* 14(2):405–414.
21. Liu W, Han F, Smith C, Fang C (2012) Ultrafast conformational dynamics of pyranine during excited state proton transfer in aqueous solution revealed by femtosecond stimulated Raman spectroscopy. *J Phys Chem B* 116(35):10535–10550.
22. Zhu L, Liu W, Fang C (2013) Tunable sideband laser from cascaded four-wave mixing in thin glass for ultra-broadband femtosecond stimulated Raman spectroscopy. *Appl Phys Lett* 103(6):061110.
23. Funk R, Schachner H, Triquet C, Kornmann M, Lux B (1976) Coating of cemented carbide cutting tools with alumina by chemical vapor deposition. *J Electrochem Soc* 123(2):285–289.
24. Henrich VE, Cox PA (1994) *The Surface Science of Metal Oxides* (Cambridge Univ Press, Cambridge, UK).
25. Franchy R (2000) Growth of thin, crystalline oxide, nitride and oxynitride films on metal and metal alloy surfaces. *Surf Sci Rep* 38(6-8):195–294.
26. Specht M, et al. (2005) Charge trapping memory structures with Al_2O_3 trapping dielectric for high-temperature applications. *Solid State Electron* 49(5):716–720.
27. Cowell EW, et al. (2011) Advancing MIM electronics: Amorphous metal electrodes. *Adv Mater* 23(1):74–78.
28. Baes CF, Mesmer RE (1976) *The Hydrolysis of Cations* (Wiley, New York).
29. Schweitzer GK, Pesterfield LL (2010) *The Aqueous Chemistry of the Elements* (Oxford Univ Press, Oxford).
30. Seichter W, Mögel H-J, Brand P, Salah D (1998) Crystal structure and formation of the aluminium hydroxide chloride $[Al_{13}(OH)_{24}(H_2O)_{24}]Cl_{15}{\cdot}13H_2O$. *Eur J Inorg Chem* 1998(6):795–797.
31. Gatlin JT, Mensinger ZL, Zakharov LN, Macinnes D, Johnson DW (2008) Facile synthesis of the tridecameric Al_{13} nanocluster $Al_{13}(\mu_3\text{-}OH)_6(\mu_2\text{-}OH)_{18}(H_2O)_{24}(NO_3)_{15}$. *Inorg Chem* 47(4):1267–1269.
32. Wang W, Wentz KM, Hayes SE, Johnson DW, Keszler DA (2011) Synthesis of the hydroxide cluster $[Al_{13}(\mu_3\text{-}OH)_6(\mu\text{-}OH)_{18}(H_2O)_{24}]^{15+}$ from an aqueous solution. *Inorg Chem* 50(11):4683–4685.
33. Rudolph WW, Mason R, Pye CC (2000) Aluminium(III) hydration in aqueous solution. A Raman spectroscopic investigation and an *ab initio* molecular orbital study of aluminium(III) water clusters. *Phys Chem Chem Phys* 2(22):5030–5040.
34. Liu W, Zhu L, Fang C (2012) Observation of sum-frequency-generation-induced cascaded four-wave mixing using two crossing femtosecond laser pulses in a 0.1 mm beta-barium-borate crystal. *Opt Lett* 37(18):3783–3785.
35. Wang W, Chang I-Y, Zakharov L, Cheong PH-Y, Keszler DA (2013) $[Sc_2(\mu\text{-}OH)_2(H_2O)_6(NO_3)_2](NO_3)_2$: Aqueous synthesis and characterization. *Inorg Chem* 52(4):1807–1811.
36. Roothaan CCJ (1951) New developments in molecular orbital theory. *Rev Mod Phys* 23(2):69–89.
37. Francl MM, et al. (1982) Self-consistent molecular orbital methods. XXIII. A polarization-type basis set for second-row elements. *J Chem Phys* 77(7):3654–3665.
38. Tomasi J, Mennucci B, Cammi R (2005) Quantum mechanical continuum solvation models. *Chem Rev* 105(8):2999–3093.
39. Frisch MJ, et al. (2009) *Gaussian 09, Revision B.01* (Gaussian, Inc., Wallingford, CT).